Cirrus Microphysical Properties from Stellar Aureole Measurements, Phase I

Final Report
DOE Funding Opportunity: DE-FOA-0000676
Topic: 31g
CFDA Number: 81.049
Phase I grant: DE-SC0006325
submitted by

Visidyne, Inc.
99 South Bedford Street, Suite # 107
Burlington, MA 01803
Principal Investigator: John DeVore
Co-Investigator: Joe Kristl
Co-Investigator: Saul Rappaport (Consultant)

Visidyne Control Number: VI-5749
Date: April 20, 2012

1. Executive Summary

Research Contribution. Atmospheric particles act to cool the Earth by reflecting incoming solar radiation if they are small (e.g., aerosols), and they can either cool or warm the earth through solar reflection in addition to thermal absorption and emission if they are large (e.g., cirrus) depending upon their altitude. While knowledge of the impact of aerosols on climate change has improved significantly due to the routine, ground-based, sun photometer measurements made at aerosol robotic network (AERONET) sites world-wide, the impact of cirrus cloud particles is much less certain because they occur high in the atmosphere and are more difficult to monitor. Recent work employed measurements of the solar aureole profiles caused by cirrus particles to retrieve the distributions of small to moderate size particles during the daytime. Phase I investigated the extension of this technique to nighttime and to larger, more thermally significant, particles. The project results are encouraging, holding the promise to improve the monitoring of the impacts of cirrus clouds on climate change by developing cost-effective technology to retrieve the microphysical properties of cirrus clouds using relatively inexpensive ground-based measurements.

Technical Effectiveness and Economic Feasibility. Phase I demonstrated the measurement of starlight diffraction in the angular range from $\lesssim 0.03^\circ$ to $\sim 0.2^\circ$ (nearly the radius of the moon) from stars, corresponding to the size range from ~ 200 μm to $\gtrsim 1500$ μm. The aureoles had very distinctive profiles that were well modeled using a simple particle size distribution, providing information that is of intrinsic interest to both cloud scientists and climatologists. The use of stellar aureoles has advantages over in-situ measurements in that (i) it can be carried out on virtually any night when thin cirrus clouds are visible, (ii) it is relatively inexpensive to implement, and (iii) the measurements do not disturb the cloud environment or the particles themselves.

Public Benefit. Development of an autonomous stellar aureole measurement instrument could enhance existing, groung-based climate monitoring networks. This would fill a gap in the information on cirrus clouds necessary for assessing, monitoring, and modeling their climate impact. The aureole approach to monitoring cirrus will provide one of the few inexpensive and portable methods available to retrieve cirrus particle microphysical properties from ground-based observations and can do for cirrus clouds what sun photometry in AERONET and other networks has done for aerosols.

1.1. Key Words

Aerosols, Cirrus Ice Crystal Size Distributions, Climate Change, Stellar Aureole Measurement, Solar Aureole Measurement

2. Goals and Accomplishments

The overall goal of Phase I was to demonstrate the retrieval of cirrus particle size distributions (PSDs) at night from measurements of stellar aureole radiance profiles. Based on previous SBIR work we had already demonstrated cirrus PSD retrieval from measurements of solar aureole profiles and had developed a commercial solar aureole measurement (SAM) instrument (DeVore et al., 2009). The SAM instrument is now in its fourth generation and has recently found application in solar energy research (Wilbert et al., 2011).

SAM measures solar aureoles in the angular range from $\sim 0.7^\circ$ to $\sim 8^\circ$, which corresponds to particles in the size range from ~ 50 μm to ~ 5 μm. The limit on the large size (small angle) end is a result of the size of the solar disk itself and technical difficulties in making measurements close to it since it is many orders of magnitude brighter than the aureole. Although the Moon provides an alternative to the Sun, we think that stars provide the best sources and that planets may have some utility as well. The angular size of the Moon is basically the same as that of the Sun and therefore does not allow for retrieving information on large particles that comes from measurements at small angles. Moreover both the Moon and planets limit where in the sky measurements can be made, whereas suitable stars are distributed across the entire sky. The instrumental challenges for stellar aureole measurements are different from those for the Sun. At the large particle end the instrumental and atmospheric point spread function (PSF) limits the measurement of cirrus diffracted radiance at small angles; and at the small particle end detector noise and scattered light, e.g., cityshine, provide a noise floor at large angles.

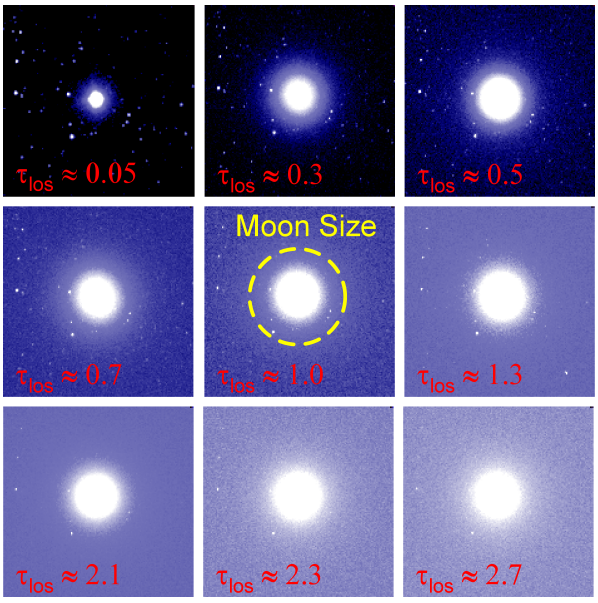

Fig. 1.— Images of aureoles around the star Capella in the astronomical S II band (672 nm) the evening of 16 Dec 2011 annotated with the cirrus optical thickness along the line of sight τ_{los} as measured by a second camera.

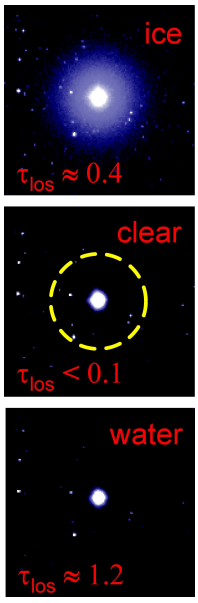

Fig. 2.— Images of the star Capella in the astronomical S II band (672 nm) through different cloud conditions the evening of 11 Jan 2012 annotated with the particulate optical thickness along the line of sight τ_{los} as measured by a second camera.

2.1. Measurement Goal

The Phase I research succeeded in demonstrating the technical feasibility of measuring aureoles around stars. Fig. 1 shows a montage of images of aureoles around the star Capella. The images are annotated with the cirrus optical thickness τ_{los} along the line of sight measured by a second camera. As the value of τ_{los} increases the apparent size and intensity of the aureole increases. The dashed yellow circle shows the size of the moon for comparison. The overall brightening of the background represents a combination of the "wings" of the aureoles, scattering of cityshine from the greater Boston area, and detector noise. Fig. 2 compares the images of the star Capella as seen through cirrus, clear sky, and a water cloud. Note that despite the fact that τ_{los} in this case is close to the value that should maximize aureole radiance (see below), the water cloud does not produce a discernable aureole because of the small size of the droplets relative to the wavelength of visible light. (Since the color scalings applied in the two sets of figures differ slightly, one should not place any particular interpretation on the light blue versus black background shading.)

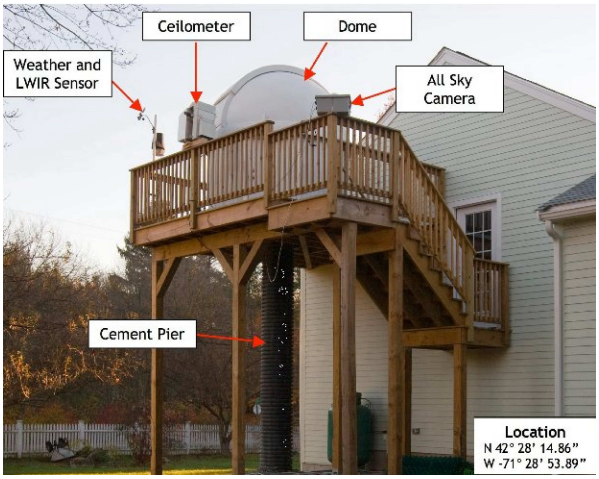

Fig. 3.— West Acton Observatory where the stellar aureole data were collected for Phase I.

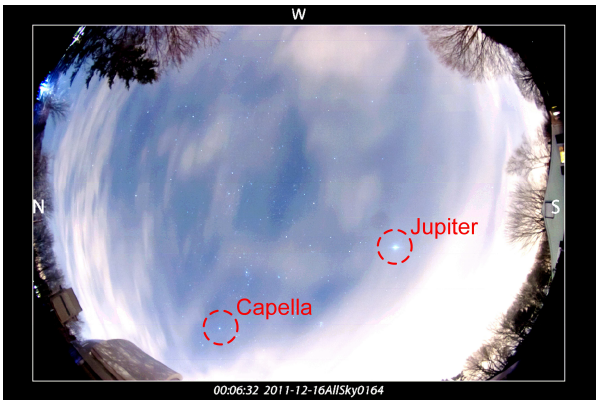

Fig. 4.— Example allsky image from the evening of 16 Dec 2011 showing the location of the star Capella and planet Jupiter.

The Phase I effort collected an extensive stellar aureole dataset at a Visidyne measurement site in Acton, MA (Fig. 3). Approximately 42 hours of stellar aureole data from 17 nights between 19 Jun 2011 and 26 Feb 2012 were collected in a narrow 5 nm band around 672 nm, using multiple exposures to extend the dynamic range. Targets ranged from bright planets such as Jupiter down to magnitude 3 stars. Sky conditions varied from clear to $\tau_{los} \approx 5$ with primarily cirrus and some water clouds. Supporting data include simultaneous τ_{los} from a second camera, all-sky imagery, laser cloud altimetry, and both local and synoptic weather data. Fig. 4 shows a typical image from the allsky camera with targets identified through the cirrus cloud. The Phase I aureole database has provided both data for analysis and valuable lessons in equipment and experimental requirements for efficient aureole measurements.

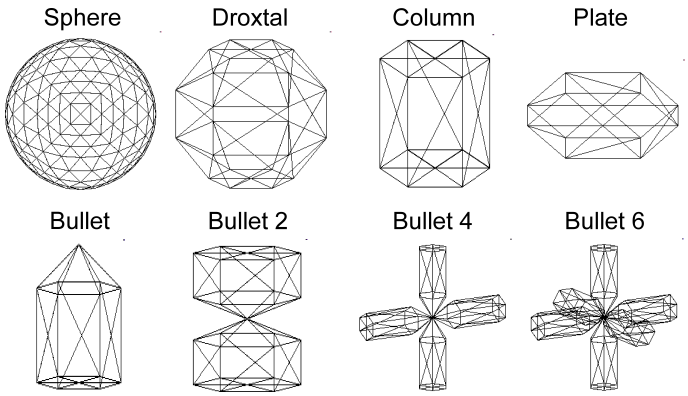

Fig. 5.— Triangular facetized surfaces used to represent 8 different crystal habits. The sphere is included for comparison with the Airy function solution for diffraction from a circular aperture.

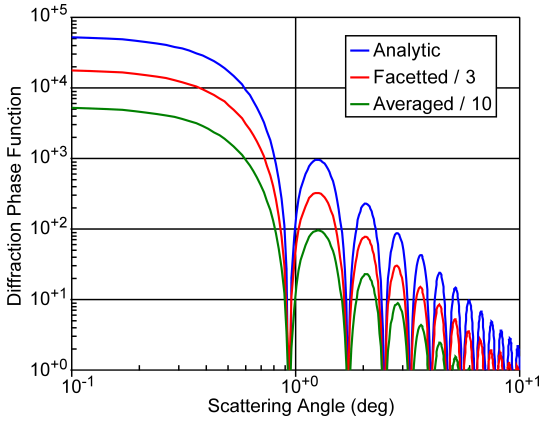

Fig. 6.— Diffraction phase functions calculated for a sphere with diameter 50 μm using the Airy function (the blue line), the facetized sphere with 1 orientation (the red line), and the facetized sphere averaged over orientations (the green line). The curves have been arbitrarily separated because they overlay each other nearly exactly.

2.2. Measurement Interpretation Goal

Diffraction is the dominant mechanism involved in forming aureole profiles (e.g., DeVore et al., 2009). Since the angles involved in stellar aureole measurements tend to be smaller than the size of the Sun, and hence smaller than the angles measured in solar aureoles, more care must be taken in the interpretation of the profiles. Ice crystals in the sensitive size range for solar aureoles tend to be compact, e.g., droxtals, and hence are well approximated as spheres. However, modeling larger ice crystals requires more complex shapes (e.g., Baum et al., 2005).

Consider diffraction from the 8 crystal habits shown in Fig. 5. We facetized the crystal surfaces using triangles. We projected the triangular facets onto the plane normal to the direction of the incident light and then calculated the diffraction pattern for the projected surface. We averaged the diffraction pattern over crystal orientations to generate a phase function representing randomly oriented crystals, which, of course, is asimuthally symmetric and a function of scattering angle only. Although not representative of a naturally occuring ice crystal we included the spherical shape both as an approximation for small ice crystals and to check our calculation of the diffraction patterns against the well-known Airy function solution (e.g., DeVore et al., 2009) as shown in Fig. 6. The droxtal shape has been used to represent small, compact ice crystals (e.g., Yang et al., 2003). While columns, plates, and bullets are observed, aggregations of bullets are more commonly used to represent the larger ice crystals in cirrus.

Fig. 7 compares calculations of the diffraction phase functions for the 8 crystal habits (shown in Fig. 5), all with the *same maximum size*, and with random orientations. The diffraction phase functions are similar with plateaus at small scattering angles followed by power-law forms with slopes of ~ -3; the oscillations in the power-law forms tend to smooth out when they are aver-

aged over distributions of particle sizes and/or shapes, but the magnitudes vary by a factor of 5. We found that diffraction phase functions for particles with the *same volumes* exhibited a factor of 3 variability versus crystal habit. For particles with the *same ratios of their volumes to their average projected areas*, the variability is over an order of magnitude. In other words, none of these measures of particle size proves self-consistent or useful for aureole work. However, particles with the *same average projected areas* are very similar as can be seen in Fig. 8, prompting us to define the "area diameter" as the diameter of the circle with the same area as that of the average over orientations of the particle projection.

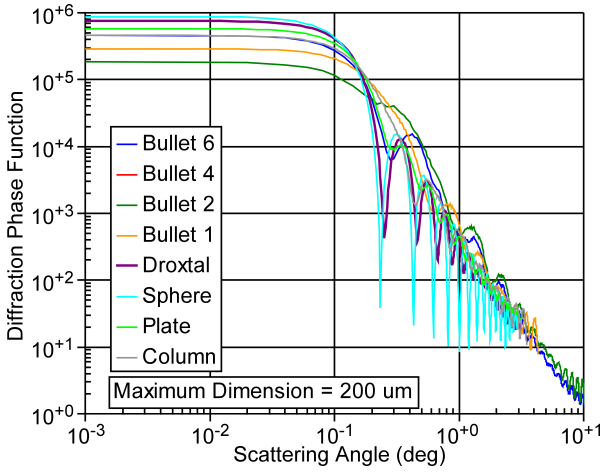

Fig. 7.— Diffraction phase functions calculated for the 8 crystal habits with maximum dimension = 200 μm.

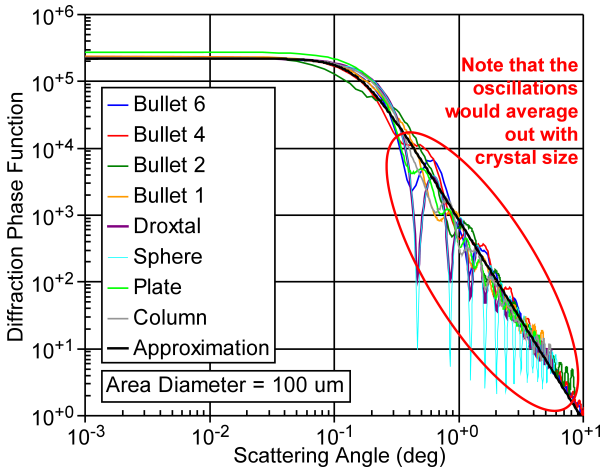

Fig. 8.— Diffraction phase functions calculated for the 8 crystal habits with area diameter = 100 μm.

The area diameter $\mathcal{D}$ therefore appears to be a useful measure of ice crystal size. From its definition and the fact that the extinction cross section σ_{ext} is twice the projected area of a particle when its size is sufficiently larger than the wavelength of light, we find that:

$$\sigma_{ext}(\mathcal{D}) \;=\; 2\frac{\pi\mathcal{D}^2}{4} \tag{1}$$

We have devised the following simple, convenient, analytic approximation to the diffraction phase function $P(\theta, \mathcal{D})$:

$$P(\theta, \mathcal{D}) \;\approx\; \frac{1}{2}\frac{(\pi\mathcal{D}/\lambda)^2}{[1+(\pi\mathcal{D}\,\xi/\lambda)^3\theta^3]} \tag{2}$$

where λ is the wavelength of the light and the constant $\xi \equiv \pi^{\frac{1}{2}}/3^{\frac{3}{4}} \approx 0.78$. The black line in Fig. 8 shows how well this approximation fits the diffraction calculations.

2.3. PSD Retrieval Goal

The phase function $P(\theta)$ representing the average over all particle sizes and habits is given by the following integral:

$$P(\theta) \;=\; \frac{\int_0^\infty \sigma_{ext}(\mathcal{D})\; P(\theta,\mathcal{D})\; N(\mathcal{D})\; d\mathcal{D}}{\int_0^\infty \sigma_{ext}(\mathcal{D})\; N(\mathcal{D})\; d\mathcal{D}} \;=\; \frac{\int_0^\infty \sigma_{ext}(\mathcal{D})\; P(\theta,\mathcal{D})\; N(\mathcal{D})\; d\mathcal{D}}{\tau_{los}} \tag{3}$$

where the extinction (rather than the scattering) cross section has been used and $N(\mathcal{D})$ is the differential number density of particles per unit area diameter.

Since they provide both simplicity and flexibility, gamma distributions are occasionally used to describe cirrus particle size distributions (e.g., Baum et al., 2005):

$$N(\mathcal{D}) \;=\; N_0\; \mathcal{D}^{\mu}\; e^{-\mathcal{D}/\mathcal{D}_0} \tag{4}$$

Three free parameters, normalization constant N_0, power μ, and size scale $\mathcal{D}_0$, allow for a wide range of distribution shapes. For simplicity here, we set $\mu = 0$, but return later to comment on how nonzero μ can be included:

$$N(\mathcal{D}) \;=\; N_0\; e^{-\mathcal{D}/\mathcal{D}_0} \tag{5}$$

Using σ_{ext}, N_0 is related to τ_{los} as follows:

$$N_0 \;=\; \frac{\tau_{los}}{\pi \mathcal{D}_0^3} \tag{6}$$

Substitution of Eqns. 1, 2, and 5 into Eqn. 3 gives:

$$P(\theta) \;=\; \frac{1}{\tau_{los}} \int_0^\infty \frac{\pi \mathcal{D}^2}{2}\; P(\theta,\mathcal{D})\; N_0\; e^{-\mathcal{D}/\mathcal{D}_0}\; d\mathcal{D} \tag{7}$$

When Eqn. 2 for $P(\theta,\mathcal{D})$ is substituted into Eqn. 7 the result can be expressed in terms of hypergeometric functions, but is not very insightful. Rather, we approximated this integral by first solving it in the limits of small θ and large θ, and then smoothly joining the resulting two analytic solutions as follows:

$$P(\theta) \;\approx\; \frac{6\;\pi^2\;\mathcal{D}_0^2}{\lambda^2} \left[\frac{1}{1 + \frac{24\;\xi^3\;\pi^3\;\mathcal{D}_0^3}{\lambda^3}\;\theta^3} \right] \tag{8}$$

The result for a general value of μ yields ξ in terms of Γ functions of μ (to be discussed in our paper in preparation).

The phase function $P(\theta)$ is related to the diffracted radiance $L_A(\theta)$ as follows (e.g., Liou, 2002):

$$L_A(\theta) \;=\; \frac{P(\theta)}{4\pi}\; \tau_{los}\; e^{-\tau_{los}}\; F_s \tag{9}$$

where the single scattering albedo (the ratio of the scattering to the extinction cross sections) has been taken as 1 and F_s is the exo-atmospheric irradiance of the star. Combining Eqns. 8 and 9 yields:

$$L_A(\theta) = \frac{3\;\pi\;\mathcal{D}_0^2\;\tau_{los}\;e^{-\tau_{los}}\;F_s}{2\;\lambda^2} \left[\frac{1}{1 + \frac{24\;\xi^3\;\pi^3\;\mathcal{D}_0^3}{\lambda^3}\;\theta^3} \right] \tag{10}$$

We simplify this equation by defining two constants L_0 and θ_0 so that:

$$L_A(\theta) = \frac{L_0}{1 + (\theta^3/\theta_0^3)} \tag{11}$$

where

$$L_0 = \frac{3\,\pi\,\mathcal{D}_0^2\,\tau_{los}\,e^{-\tau_{los}}\,F_s}{2\,\lambda^2} \tag{12}$$

and

$$\theta_0 = \frac{\lambda}{24^{\frac{1}{3}}\,\xi\,\pi\,\mathcal{D}_0} \tag{13}$$

As a brief aside with important implications, we note that implicit in Eqn. 10 is the following wavelength scaling relationship:

$$L_A(\lambda_2, \theta_2 = \frac{\lambda_2}{\lambda_1}\theta_1) = \frac{\lambda_1^2}{\lambda_2^2}\,\frac{F_s(\lambda_2)}{F_s(\lambda_1)}\,L_A(\lambda_1, \theta_1) \quad \text{if } \theta_1 \ll 1 \text{ and } \theta_2 \ll 1 \tag{14}$$

We note that Eqn. 14 can be shown to hold quite generally.

Eqn. 10 provides a connection between measurements of starlight diffracted by cirrus and the size distribution of the ice crystals. However, there are two other significant contributions to stellar aureole radiance: the instrumental/atmospheric point spread function and background radiance and noise. While it suffices to model the latter as a uniform, additive component, the former tends to be sharply peaked as $\theta \to 0$. Fortunately it has been found that the Moffat function (Moffat, 1969) does an excellent job of modeling the point spread function PSF(θ):

$$\text{PSF}(\theta) = \frac{I_0}{[1 + (\theta/\theta_{psf})^2]^\beta} \tag{15}$$

where I_0 is the stellar radiance at $\theta = 0$, and θ_0 and β are fitting parameters.

The measured stellar aureole profile can then be fit with the sum of three functions, representing the point spread function, a uniform background, and diffraction by cirrus ice crystals. We employ the Levenberg-Marquardt algorithm (e.g., Press et al., 1992) to determine the six parameters (3 for PSF(θ), 1 for the background, and 2 for $L_A(\theta)$) representing the best fit in a least squares sense to stellar aureole measurements.

After routine astronomical image data reduction (offset, bias, and flat field corrections), the center of the bright star image was located, and the aureole profile was measured from the radiances in a series of annuli concentric with the star. The larger numbers of pixels contained in each annulus, with increasing radial distance, significantly reduced the image noise and extended the measurement dynamic range. The counts within each annulus were averaged and then converted into quantities similar to radiances by dividing by the pixel instantaneous field of view, the objective aperture area, and the exposure time. Fig. 9 shows an example of aureole profile measurement data (the black diamonds) around the star Capella in the early morning of 17 Dec 2011. The red line shows the least-squares fit and the orange, green, and blue lines represent the individual physical components in the fit.

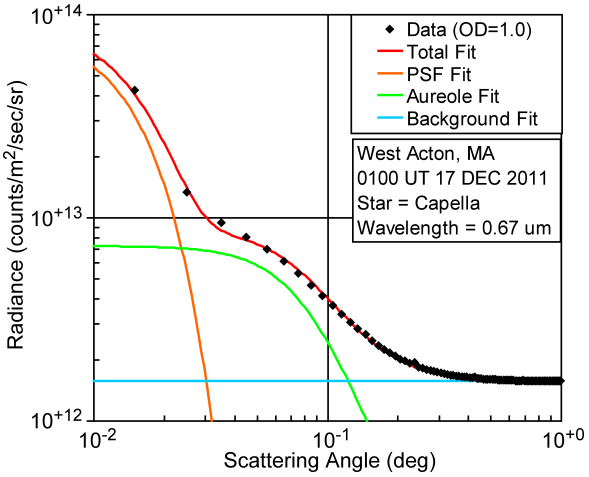

Fig. 9.— Example aureole profile and least-squares fit for the star Capella at 0100 UT on 17 Dec 2011.

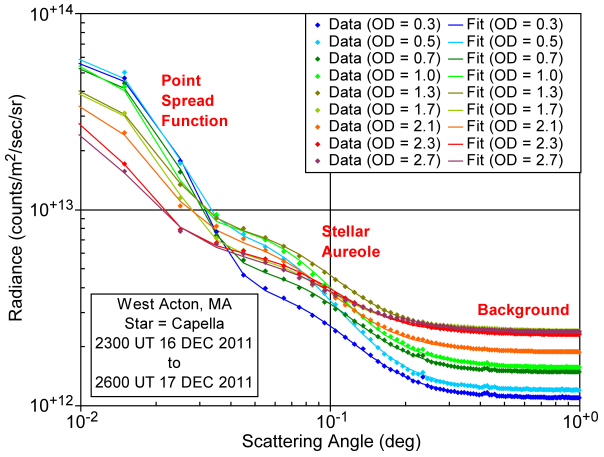

Fig. 10.— Further examples of aureole profiles and least-squares fits for the star Capella from the evening of 16 Dec 2011 annotated by the cirrus optical depth.

From the datasets we have collected in Phase I, some 30% of which have been analyzed in detail, we show a few illustrative examples in the following figures. Fig. 10 shows more measurement data and fits from the evening of 16 Dec 2011. The PSF and background magnitudes are anti-correlated as one might expect, with the PSF being brightest when τ_{los} is least while the background is brightest when τ_{los} is greatest. Fig. 11 shows another set of example aureole profiles and data fits from another day (the early morning of 27 Nov 2011), when the cirrus clouds were present with a wide range of optical thicknesses ($\tau_{los} \sim 0.1$ to ~ 3). Fig. 12 is analogous to Fig. 9 but for the planet Jupiter early in the morning of 27 Nov 2011. Note that in this case the aureole profile does not drop down to the background level until about 0.5°, providing a potentially useful increase in particle size measurement range down to ~ 100 μm.

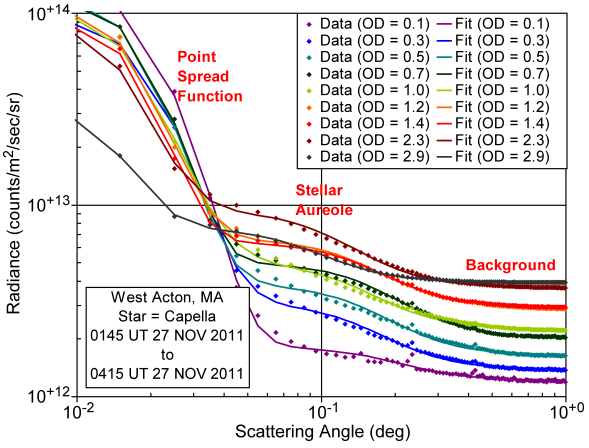

Fig. 11.— Examples of aureole profiles and least-squares fits for the star Capella from the early morning of 27 Nov 2011 annotated by the cirrus optical depth.

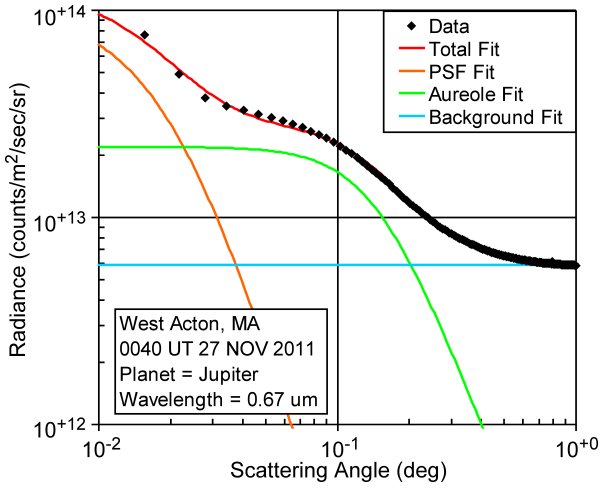

Fig. 12.— Example aureole profile and least-squares fit for the planet Jupiter at 0040 UT on 27 Nov 2011.

Fig. 13 shows the diffraction components of the aureole profiles in Fig. 10. Note that the diffracted radiance peaks for $\tau_{los} \approx 1$ as is expected from simply differentiating $L_A(\theta)$ (see Eqn. 9) with respect to τ_{los} and setting the derivative to zero.

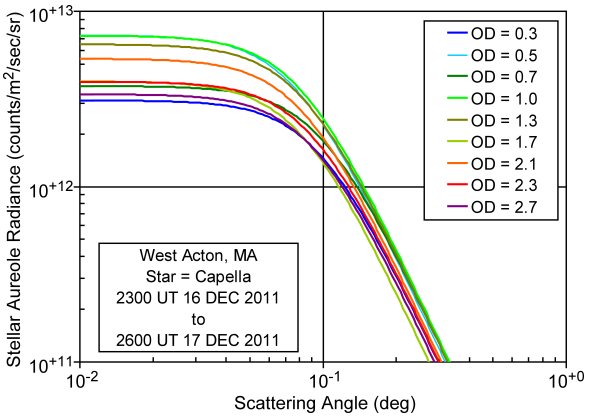

Fig. 13.— Illustrative diffraction profiles corresponding to the aureole profiles in Fig. 10.

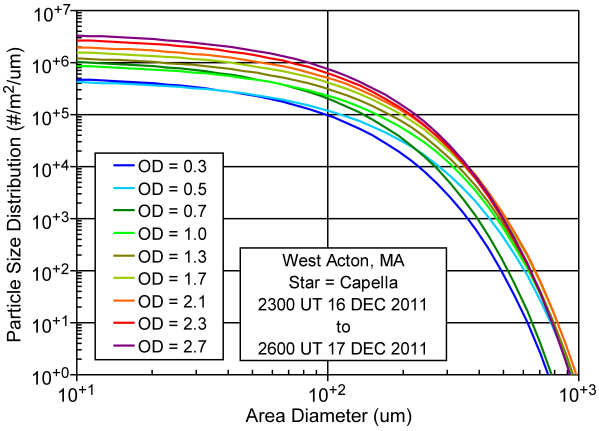

Fig. 14.— Particle size distributions calculated from the diffraction profiles in Fig. 13.

We find the particle size distribution from the fitting parameters and τ_{los}. N_0 comes from Eqn. 6 and $\mathcal{D}_0$ comes from inverting Eqn. 13:

$$\mathcal{D}_0 = \frac{\lambda}{24^{\frac{1}{3}}\,\xi\,\pi\,\theta_0} \tag{16}$$

It turns out that the fitting parameter L_0 is nearly redundant with $\mathcal{D}_0$ and that it is best used to define F_s (if it is needed) since this parameter would require an absolute calibration of the cameras used, whereas the other parameters, including τ_{los} require only calibration for linearity of response with respect to the radiance. Fig. 14 shows the particle size distributions derived from the diffraction profiles shown in Fig. 13. There is some variability in the shape of the profiles for the two thinnest cases. Otherwise, $N(\mathcal{D})$ increases with τ_{los}.

The stellar aureoles that we have measured, as illustrated in Figs. 9, 10, and 11, are typically based on stacks (i.e., sums) of 30-sec images. The stack of images allows for better suppression of statistical fluctuations in the outer portions of the stellar aureole; however, the innermost portions of the stellar profile, which represent the instrument PSF, tend to saturate the CCD wells. In spite of this saturation, we were able to successfully fit the PSF portion with either a Gaussian or Moffat function. However, to the extent that recording and fitting an unsaturated PSF is important, this can easily be accomplished by recording a set of stellar images with a range of exposures. As an example, Fig. 15 shows an aureole profile assembled by compositing individual images with exposures of 0.0001, 1, and 30 sec duration (taken the evening of 26 Feb 2012 at our observatory in West Acton). The stellar profile now spans a range of two full decades of unsaturated radiances, and extends the PSF sampling in to within $\sim 10''$ of the stellar image center. If this is ultimately deemed important in aiding the extraction of aureoles over a wider dynamic range in angle, it is easily implemented, mostly at the cost of additional bookkeeping and image storage.

Finally we note that the forms of $P(\theta)$ in Eq, 8 and the Moffat function representing the PSF (Eqn. 15) might be nearly of the same form if the parameter β were to take on a value of $\sim 3/2$. However, our Phase I measurements over a very wide range of optical depths (from ~ 0 to ~ 3) show that β also varies over a range of a couple of decades. Thus, we have clearly demonstrated that the instrument/atmospheric PSF and the aureole profile are rather distinct.

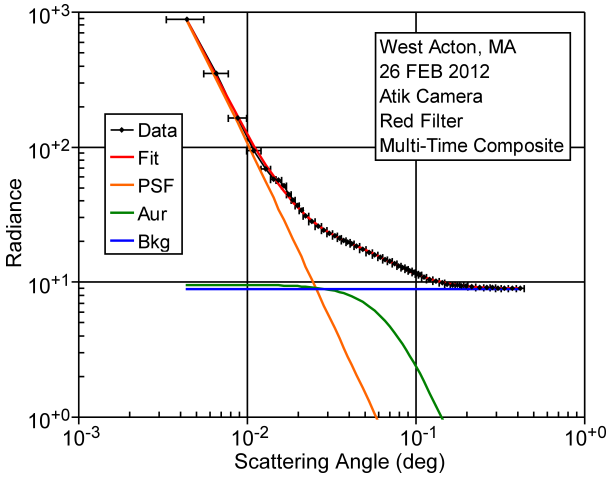

Fig. 15.— Example stellar aureole profile derived by compositing images with exposures of 0.0001, 1, and 30 sec.

3. Phase I Summary

In summary, the technical objectives of Phase I have been met. (1) We have collected a useful stellar aureole database covering different atmospheric conditions and cloud optical thicknesses. (2) Stellar aureole profiles have clearly been detected and measured through a wide range of cloud conditions. (3) The aureole profiles can be followed out to $\sim 0.2^\circ$ from stars ($\sim 0.5^\circ$ from Jupiter). (4) The stellar aureoles from cirrus have very distinctive profiles, being typically flat out to a critical angle, followed by a steep power-law decline with a slope of ~ -3. (5) The profiles for the nights that have been analyzed in detail are well modelled using exponential size distributions (Eqn. 5) coupled with the simple analytic approximation in Eqn. 2 for individual crystal diffraction phase functions. (6) The critical angle (θ_0) in the data profiles presented here is $\sim 0.12^\circ$. This indicates that $\mathcal{D}_0$ ranges from ~ 150 to ~ 200 μm on the two particular nights for which we presented multiple profiles. Similar analyses of the other datasets in our collects establish $\mathcal{D}_0$ for a number of nights using a robust yet relatively simple algorithm.

Interesting theoretical results include (a) a simple, fast, yet flexible approach to calculating diffraction from complex ice crystal shapes using triangular facetization and 2-D Fourier transforms, (b) the discovery that the area diameter ($\mathcal{D}$) provides a useful way of describing ice crystal size leading to a simple, approximate, "universal" phase function, and (c) the derivation of a wavelength-size scaling relationship (Eqn. 14) for cirrus aureole profiles.

The stage has been set to proceed to validating the PSD retrievals using comparisons with cirrus optical property retrievals from other ground-based instruments, and developing an instrument for the routine, automatic measurement of thin cirrus microphysical properties in Phase II.

4. Products and Technology Transfer

4.1. Publications

We are currently drafting an article for the Journal of Geophysical Research. Also, we presented a poster at the 2012 ASR Science Team Meeting. The brochure version of this poster is available from the conference web site
(http://asr.science.energy.gov/meetings/stm/posters/poster_pdf/2012/P000531.pdf).

4.2. Web Site

The web site of the West Acton Observatory, where our Phase I stellar aureole measurements were collected, discusses this work briefly and is planned to provide access to the data and other products of this research. It can be accessed at http://www.westactonastro.com/cloud-stellar-aureoles.html. The SAM work is older and more mature. Access to it is provided through Visidyne's web site at http://www.visidyne.com/SAM/index.htm.

4.3. Networks and Collaborations

Researchers at the University of Wisconsin, Madison have expressed interest in collaboration on the stellar aureole research. Our Phase II proposal includes support for a Wisconsin graduate student under the supervision of Dr. Robert Holz to operate new prototype stellar aureole instruments that we would design and build and to compare the stellar aureole ice crystal PSD retrievals with measurements and optical property retrievals from their High Spectral Resolution Lidar (HSRL) and Atmospheric Emitted Radiation Interferometer (AERI).

4.4. Inventions, Patent Applications, Etc.

None under Phase I.

4.5. Other Products.

As noted in some detail in §2.1 during Phase I we collected a stellar aureole database, which has provided clean datasets for analysis. The database collection effort also afforded valuable lessons in equipment and experimental requirements for efficient aureole measurements. Our analysis effort has produced some potentially very valuable algorithms and insights.

5. Computer Modeling

Our Phase I work did involve a significant component of computer modeling in regard to the particle scattering phase functions and calculations of the expected stellar aureole profiles. However, the primary goal of the project was the development of a new instrument and specific analysis techniques and algorithms for measuring and analyzing stellar aureoles.

6. Conclusion

In conclusion we believe that the stage has been set for a Phase II project (1) to proceed to validating the use of stellar aureole measurements for retrieving cirrus PSD retrievals using comparisons with optical property retrievals from other, ground-based instruments and (2) to develop an instrument for the routine, automatic measurement of thin cirrus microphysical properties. In the process we would (3) endeavor to extend the angular range of stellar aureole measurement to both smaller and larger angles (corresponding to larger and smaller particles) and (4) investigate alternative algorithms for inverting size distributions from stellar aureole measurements.

6.0.1. Bibliography and References Cited

Baum, B., P. Yang, A.J. Heymsfield, S. Platnick, M. D. King, Y.-X. Hu, & S.T. Bedka, 2005, "Bulk Scattering Properties for the Remote Sensing of Ice Clouds. Part II: Narrowband Models", *J. Appl. Meteor.*, *44*, pgs 1896-1910.

DeVore, J.G., A.T. Stair, A. LePage, D. Rall, J. Atkinson, D. Villanucci, S.A. Rappaport, P.C. Joss, & R.A. McClatchey, 2009, "Retrieving Properties of Thin Clouds from Solar Aureole Measurements", *J. Atmos. Ocean. Tech.*, *26*, pgs 2531-2548.

Liou, K.-N., 2002, *An Introduction to Atmospheric Radiation, Second Edition*, Academic Press, San Diego.

Moffat, A.F.J., 1969, "A Theoretical Investigation of Focal Stellar Images in the Photographic Emulsion and Application to Photographic Photometry", *Astron. & Astrophys.*, *3*, pgs 455-461.

Press, W.H., S.A. Teukolsky, W.T. Vettering, and B.P. Flannery, 1992, *Numerical Recipes in Fortran, The Art of Scientific Computing, Second Edition*, Cambridge University Press, Cambridge, UK.

Wilbert, S., B. Reinhardt, J. DeVore, M. ROger, R. Pitz-Pall, and C. Gueymard, 2011, "Measurement of Solar Radiance Profiles With the Sun and Aureole Measurement System (SAM)", *Proc. SolarPACES Conf., Granda Spain"*.

Yang, P., B.A. Baum, A.J. Heymsfield, X. Hu, H.-L. Huang, S.-C. Tsay, and S. Ackerman, 2003, "Single-Scattering Properties of Droxtals", *J. Quant. Spec. Rad. Tran.*, *79*, pgs 1159-1169.